



CO depletion in infrared dark clouds

Downloaded from: <https://research.chalmers.se>, 2026-03-17 06:18 UTC

Citation for the original published paper (version of record):

Cosentino, G., Tan, J., Gainey, C. et al (2026). CO depletion in infrared dark clouds. *Astronomy and Astrophysics*, 705. <http://dx.doi.org/10.1051/0004-6361/202557102>

N.B. When citing this work, cite the original published paper.

CO depletion in infrared dark clouds

G. Cosentino^{1,2,*}, J. C. Tan^{3,4}, C. Gainey⁵, C. Y. Law⁶, C.-J. Hsu³, D. Xu⁴, W. Lim⁷, I. Jiménez-Serra⁸,
A. T. Barnes², F. Fontani^{6,9,10}, J. D. Henshaw¹¹, P. Caselli¹⁰, and S. Viti¹²

- ¹ Institut de Radioastronomie Millimétrique, 300 Rue de la Piscine, 38400 Saint-Martin-d'Hères, France
² European Southern Observatory, Karl-Schwarzschild-Strasse 2, 85748 Garching, Germany
³ Department of Space, Earth and Environment, Chalmers University of Technology, 412 96 Gothenburg, Sweden
⁴ Department of Astronomy, University of Virginia, 530 McCormick Road, Charlottesville, VA 22904-4325, USA
⁵ Department of Astronomy, Yale University, New Haven, CT 06511, USA
⁶ INAF Osservatorio Astronomico di Arcetri, Largo E. Fermi 5, 50125 Florence, Italy
⁷ California Institute of Technology, Pasadena, CA 91125, USA
⁸ Centro de Astrobiología (CSIC/INTA), Ctra. de Torrejón a Ajalvir km 4, Madrid, Spain
⁹ Laboratory for the study of the Universe and eXtreme phenomena (LUX), Observatoire de Paris, 5, place Jules Janssen, 92195 Meudon, France
¹⁰ Max Planck Institute for Extraterrestrial Physics, Giessenbachstrasse 1, 85748 Garching bei München, Germany
¹¹ Astrophysics Research Institute, Liverpool John Moores University, 146 Brownlow Hill, Liverpool L3 5RF, UK
¹² Leiden Observatory, Leiden University, PO Box 9513, 2300 RA Leiden, The Netherlands

Received 4 September 2025 / Accepted 28 October 2025

ABSTRACT

Context. Infrared dark clouds (IRDCs) are cold, dense structures that are likely representative of the initial conditions of star formation. Many studies of IRDCs employ CO to investigate cloud dynamics, but CO can be highly depleted from the gas phase in IRDCs, which affects its fidelity as tracer. The CO depletion process is also of great interest in astrochemistry because CO ice in dust grain mantles provides the raw material for the formation of complex organic molecules.

Aims. We study CO depletion towards four IRDCs to investigate its correlation with the H₂ number density and dust temperature, calculated from *Herschel* far-infrared images.

Methods. We used ¹³CO $J = 1 \rightarrow 0$ and $2 \rightarrow 1$ maps to measure the CO depletion factor, f_D , across IRDCs G23.46-00.53, G24.49-00.70, G24.94-00.15, and G25.16-00.28. We also considered a normalised CO depletion factor, f'_D , which takes a value of unity, that is, no depletion, in the outer lower-density and warmer regions of the clouds. We then investigated the dependence of f_D and f'_D on the gas density, n_H , and dust temperature, T_{dust} .

Results. The CO depletion rises as the density increases and reaches maximum values of $f'_D \sim 10$ in some regions with $n_H \gtrsim 3 \times 10^5 \text{ cm}^{-3}$, although with significant scatter at a given density. We find a tighter, less scattered relation of f'_D with temperature that rapidly rise for temperatures $\lesssim 18 \text{ K}$. We propose a functional form $f'_D = \exp(T_0/[T_{\text{dust}} - T_1])$ with $T_0 \simeq 4 \text{ K}$ and $T_1 \simeq 12 \text{ K}$ to reproduce this behaviour.

Conclusions. We conclude that CO is strongly depleted from the gas phase in cold, dense regions of IRDCs. This means that if it is not accounted for, CO depletion can lead to an underestimation of the total cloud masses based on CO line fluxes by factors up to ~ 5 . These results indicate a dominant role for thermal desorption in setting near equilibrium abundances of gas-phase CO in IRDCs and provide important constraints for astrochemical models and the chemodynamical history of gas in the early stages of star formation.

Key words. ISM: abundances – ISM: clouds – ISM: kinematics and dynamics – ISM: lines and bands – ISM: molecules

1. Introduction

Infrared dark clouds (IRDCs) are cold ($T \lesssim 20 \text{ K}$; Pillai et al. 2006), dense ($n_H \gtrsim 10^4 \text{ cm}^{-3}$; Butler & Tan 2012) and highly extinguished ($A_V \sim 10\text{--}100 \text{ mag}$) regions of the interstellar medium (ISM) that are known to harbour the conditions of star and star cluster formation. First detected as dark features against the mid-infrared (MIR) Galactic background (Perault et al. 1996; Egan et al. 1998), IRDCs show low levels of star formation activity, and their mass surface densities are similar to those of massive star-forming regions (Tan et al. 2014). Furthermore, IRDCs host cold, dense, deuterated pre-stellar cores, that is, the earliest phase of massive star formation (Tan et al. 2013; Kong et al. 2017). For

all these reasons, IRDCs have long been regarded as the birth places of massive stars and star clusters (Rathborne et al. 2006; Foster et al. 2014; Pillai et al. 2019; Moser et al. 2020; Yu et al. 2020).

Despite this importance, the mechanisms that trigger star formation in these objects are still unclear (e.g. Tan 2000; Tan et al. 2014; Hernandez & Tan 2015; Peretto et al. 2016; Retes-Romero et al. 2020; Morii et al. 2021). Theoretical models and simulations have suggested that star formation can be efficiently ignited within IRDCs as a consequence of dynamical compression and gravitational instability of the gas. In current theories, IRDCs have been proposed to form as the shock-compressed layer in the collision between pre-existing giant molecular clouds (GMCs; e.g. Tan 2000; Tasker & Tan 2009; Tan 2010; Suwannajak et al. 2014; Wu et al. 2015, 2017; Li et al. 2018; Fortune-Bashee et al. 2024), with the collision being a consequence of the GMC

* Corresponding author: cosentino@iram.fr

orbital motion in a shearing Galactic disk. Other models also involve the formation from compressive collisions, but driven by momentum from stellar feedback (e.g. [Inutsuka et al. 2015](#)). Still other models invoke the IRDCs and dense clump formation as part of the same processes of hierarchical gravitational collapse that forms the surrounding GMCs (e.g. [Vázquez-Semadeni et al. 2019](#)). All these mechanisms are expected to leave different imprints on the gas dynamical properties in the formed IRDCs.

Since molecular hydrogen H_2 , the primary constituent of molecular clouds, is not excited at the low temperatures of these objects, indirect methods of tracing cloud mass have been developed. Among these, CO rotational transitions and its isotopologues have been used to study the structure and kinematics of molecular clouds, assuming a certain CO to H_2 abundance ratio. For the conditions that typically prevail in IRDCs, however, CO can be strongly depleted in the gas phase by freeze-out onto dust grains (e.g. [Caselli et al. 1999](#); [Crapsi et al. 2005](#); [Fontani et al. 2006](#); [Hernandez et al. 2011](#); [Jiménez-Serra et al. 2014](#); [Sabatini et al. 2019](#); [Entekhabi et al. 2022](#)). This may cause important quantities, such as cloud mass, to be significantly underestimated.

CO depletion also has major implications for the chemistry of star-forming regions. For example, if CO is highly depleted from the gas phase, then the abundance of H_2D^+ can rise, which leads to high levels of deuteration of the remaining gas-phase species, such as N_2H^+ and NH_3 (e.g. [Dalgarno & Lepp 1984](#); [Caselli et al. 2002](#); [Fontani et al. 2006](#); [Caselli et al. 2008](#); [Kong et al. 2015](#); [Sabatini et al. 2020, 2024](#); [Redaelli et al. 2021](#); [Entekhabi et al. 2022](#); [Redaelli et al. 2022](#)). In addition, the formation of many complex organic molecules (COMs) is expected to occur within the CO ice mantles of dust grains (e.g. [Herbst & van Dishoeck 2009](#)).

The gas-phase depletion of CO is typically quantified using the so-called CO depletion factor, f_D , that is, the ratio of the expected CO column density given a CO-independent measure of the column density of H nuclei, N_H , and assuming the standard gas-phase CO abundance along a line of sight to the observed CO column density. Estimates of N_H in molecular clouds are typically made via dust continuum emission at sub-millimetre and millimetre wavelengths (e.g. [Lim et al. 2016](#)) or via mid- and near-infrared (NIR) dust extinction measurements (e.g. [Butler & Tan 2012](#); [Kainulainen & Tan 2013](#)).

On the smaller scales of cores ($\lesssim 0.1$ pc), CO depletion has been investigated towards low- (e.g. [Caselli et al. 1999](#); [Kramer et al. 1999](#); [Whittet et al. 2010](#); [Ford & Shirley 2011](#); [Christie et al. 2012](#)) and high-mass (e.g. [Fontani et al. 2006](#); [Zhang et al. 2009](#); [Fontani et al. 2012](#); [Sabatini et al. 2019](#)) examples. In both cases, high values of CO depletion factors have been reported. In particular, in high-mass pre-stellar and early-stage cores, [Fontani et al. \(2012\)](#) estimated values up to $f_D > 80$, while [Zhang et al. \(2009\)](#) found $f_D > 100$. High angular resolution observations obtained with the Atacama Large millimeter/sub-millimeter array (ALMA) of massive clumps and cores from the ASHES survey by [Sabatini et al. \(2022\)](#) showed CO depletion factors up to $\gtrsim 100$ that did not decrease from the pre-stellar to the protostellar cores.

On the larger scales of IRDCs, [Hernandez et al. \(2011\)](#) and [Hernandez et al. \(2012\)](#) used multi-transition single-dish observations of the $C^{18}O$ isotope to obtain a parsec-scale CO depletion map of IRDC G35.39-00.33. Under the assumption of local thermodynamic equilibrium (LTE) conditions, they reported values of f_D of up to ~ 3 . Towards the same cloud, [Jiménez-Serra et al. \(2014\)](#) used the LVG approximation and reported CO depletion factors of $\sim 5, 8$, and 12 in three selected positions. Similar results

were reported towards IRDC G351.77-0.51 by [Sabatini et al. \(2019\)](#). Towards IRDC G28.37+00.07, [Entekhabi et al. \(2022\)](#) reported values of f_D up to ~ 10 . [Feng et al. \(2020\)](#) investigated CO depletion towards a sample of four IRDCs and presented CO depletion maps with f_D values of up to 15. Towards the Serpens filament, [Gong et al. \(2021\)](#) reported widespread CO depletion, suggesting that the filament is young and still accreting. On larger scales, [Clarke et al. \(2024\)](#) reported CO depletion towards the giant molecular filament G214.5–1.8 already at volume densities $2 \times 10^3 \text{ cm}^{-3}$, which translates into a very low cosmic-ray ionisation rate ($\zeta \approx 2 \times 10^{-18} \text{ s}^{-1}$). Similarly, [Hirata et al. \(2024\)](#) observed parsec-scale CO depletion towards several star-forming regions associated with Canis Major OB1. The authors showed that $C^{18}O(1-0)$ under-traces dense gas at parsec scales, although it remains unclear to which extent local temperature conditions affect this behaviour. Finally, [Socci et al. \(2024\)](#) investigated the large-scale CO depletion across OMC-2 and OMC-3 and reported values that are consistent with previous measurements obtained in star-forming regions. The authors also suggested CO depletion as a viable proxy of $o\text{-}H_2D^+$. All these studies have confirmed that depletion of CO from the gas phase is significant not just towards the dense cores and clumps, but also in the inter-clump regions of IRDCs.

While it is generally known that CO depletion is affected by density and temperature variations, only a few previous studies have been dedicated to specific investigation of the dependence of f_D on these properties. In particular, [Kramer et al. \(1999\)](#) investigated the dependence of CO depletion on the dust temperature towards the dense core IC 5146. They found that their data were well fitted with the following function:

$$f_D = A \exp(T_0/T), \quad (1)$$

with $A = 0.41_{0.25}^{0.67}$ and $T_0 = 14.1 \pm 0.6$ K. We note, however, that their data covered a relatively modest range of depletion factors, that is, up to $f_D \sim 2.5$. Furthermore, their dust temperatures were estimated based on the ratio of 1.2 mm flux to NIR dust extinction (with equivalent A_V ranging up to about 30 mag, i.e. up to $\Sigma \approx 0.13 \text{ g cm}^{-2}$), which is relatively sensitive to the choice of dust opacity model.

In this work, we explore CO depletion in a sample of four IRDCs, namely G24.94-00.15, G23.46-00.53, G24.49-00.70, G25.16-00.28, which are part of a larger sample of 26 clouds ([Butler & Tan 2009, 2012](#), Cosentino et al., in prep.). This paper is organised as follows. In Section 2 we present our sample, the data, and the technical details of our observations. In Section 3, we describe the method we adopted and the analysis we performed. In Sections 4 and 5, we present and discuss our results. In Section 6 we draw our conclusions.

2. The IRDC sample

The four IRDCs studied in this work were selected from a larger sample of 16 clouds (K to Z) that will be presented in a forthcoming paper (Cosentino et al. in prep.). They extend the sample of ten IRDCs of [Butler & Tan \(2009, 2012\)](#) (labelled A to J). These 26 sources were identified as dark features against the diffuse MIR Galactic background. They were selected for being located relatively nearby (kinematic distance ≤ 7 kpc) and for showing the highest levels of contrast against the diffuse Galactic background emission as observed with Spitzer-IRAC at $8 \mu\text{m}$ ([Churchwell et al. 2009](#)).

We selected the four IRDCs, namely G24.94-00.15 (cloud O), G23.46-00.53 (cloud V), G24.49-0.70 (cloud X),

Table 1. Noise and background values for the *Herschel*-derived Σ and T_{dust} .

Cloud	σ_{Σ} (K)	$\sigma_{T_{\text{dust}}}$	Σ_{bkg}	T_{bkg}
G24.94-00.15	0.06	2	0.1	2
G23.46-00.53	0.05	2	0.1	2
G24.49-00.70	0.03	2	0.1	2
G25.16-00.28	0.02	2	0.1	2

and G25.16-0.28 (cloud Y) to probe different regimes of the mass surface density, Σ , and dust temperature, T_{dust} . In addition, these IRDCs show relatively simple kinematics (Cosentino et al., in prep.). For the four clouds, Σ and T_{dust} images were obtained from multi-wavelength *Herschel* images using the method described by Lim et al. (2016). Briefly, *Herschel*-PACS and SPIRE images at 160, 250, 350, and 500 μm were first re-gridded to match the poorest angular resolution of the 500 μm image (36"). Next, the Galactic Gaussian method of background subtraction was used (see Lim et al. 2016). The effect of this is to remove $\sim 0.1 \text{ g cm}^{-2}$ and $\sim 2 \text{ K}$ from all clouds on average in the Σ and T_{dust} images, respectively. After this, the multi-wavelength emission, re-gridded to a scale of 18" pixels (hires method of Lim et al. 2016), was fitted using a grey body function, and Σ and T_{dust} were estimated. The Σ and T_{dust} *Herschel*-derived images of the four clouds are shown in Figure 1. For each cloud, the average subtracted background, average Σ , and T_{dust} noise values are reported in Table 1. To the best of our knowledge, no previous studies have been dedicated to these clouds.

3. Observations and data

In May 2021, we used the 30m single-dish antenna at the Instituto de Radioastronomía Millimétrica (IRAM 30m; Pico Veleta, Spain) to map the $J = 2 \rightarrow 1$ rotational transition of ^{13}CO ($\nu=220.38 \text{ GHz}$) towards 16 IRDCs as an extension of the A-J sample of Butler & Tan (2012). The observations were performed in on-the-fly observing mode with an angular separation in the direction perpendicular to the scanning direction of 6". For each cloud, the central map coordinates, the map size, and the off positions are listed in Table 2. For the observations, we used the Fast Fourier transform spectrometer (FTS) set to provide a spectral resolution of 50 kHz, corresponding to a velocity resolution of 0.13 km s^{-1} at the $^{13}\text{CO}(2-1)$ rest frequency. The intensities were measured in units of antenna temperature, T_A^* , and converted into main-beam brightness temperature, $T_{\text{mb}} = T_A^*(B_{\text{eff}}/F_{\text{eff}})$, using forward and beam efficiencies of F_{eff} and B_{eff} of 0.94 and 0.61, respectively¹. The final data cubes were created using the CLASS software within the GILDAS² package and have a spatial resolution of 11" and a pixel size of $5.5'' \times 5.5''$. The achieved rms per channel per pixel is reported in Table 2.

The $^{13}\text{CO}(2-1)$ IRAM30m data were complemented using the $^{13}\text{CO}(1-0)$ cubes from the FOREST Unbiased Galactic plane Imaging survey with the Nobeyama 45-m telescope (FUGIN) survey (Umemoto et al. 2017). This survey uses the 45m antenna at the Nobeyama Radio Observatory (Japan) to map the ^{12}CO , ^{13}CO and $\text{C}^{18}\text{O } J = 1 \rightarrow 0$ transitions towards part of the first

($10^\circ \leq l \leq 50^\circ$, $|b| \leq 1^\circ$) and third ($198^\circ \leq l \leq 236^\circ$, $|b| \leq 1^\circ$) quadrants of the Galaxy. The observations were performed in on-the-fly mode with a scanning speed of $100''/\text{s}$. The publicly available cubes have $B_{\text{eff}}=0.43$, an angular resolution of $20''$, a pixel size of $8.5''$, a velocity resolution of 0.65 km s^{-1} , and an rms of 0.65 K per channel per pixel. For a more detailed description of the survey, we refer to Umemoto et al. (2017).

4. Results and discussion

4.1. Identification of the ^{13}CO emission velocity

In Figure 2 (left column), we show the $^{13}\text{CO}(1-0)$ (black) and $(2-1)$ (red) spectra averaged across the full map regions of each IRDC. Most spectra show multiple velocity components in both transitions. ^{13}CO is a very abundant species ($\chi \sim 10^{-6}$ with respect to H; e.g. Frerking et al. 1982) that probes relatively low-density molecular material in the ISM (the typical critical densities of the $J=1-0$ transition is $\sim 10^3 \text{ cm}^{-3}$; Yang et al. 2010). We now wish to discern which of these components are associated with the clouds and which simply arise from emission along the line of sight. To do this, we visually investigated the spatial correspondence and overlap between the cloud structure seen in the *Herschel*-derived maps (Figure 1) and each velocity component. From this correspondence, we identified the velocity ranges of the ^{13}CO emission associated with each cloud to be in the ranges $40-60 \text{ km s}^{-1}$ for G24.94-00.15, $58-68 \text{ km s}^{-1}$ for G23.46-00.53, $42-54 \text{ km s}^{-1}$ for G24.49-00.70, and $58-68 \text{ km s}^{-1}$ for G25.16-00.28. The $^{13}\text{CO}(1-0)$ and $(2-1)$ integrated intensity maps obtained over these velocity ranges are also shown in Figure 2. These velocity ranges are reported in Table 2, along with the corresponding integrated noise for both transitions. We note that a more detailed analysis of the gas kinematics towards these sources will be presented in a forthcoming paper.

4.2. $\Sigma_{^{13}\text{CO}}$ and T_{ex} maps

Following the method described by Hernandez et al. (2011), we used the $^{13}\text{CO}(1-0)$ and $(2-1)$ emission to map the CO depletion factor across the four clouds. In particular, we re-gridded the $^{13}\text{CO}(2-1)$ IRAM maps to match the poorer pixel size and the angular and velocity resolution of the corresponding $^{13}\text{CO}(1-0)$ FUGIN maps. We then assumed local thermodynamic equilibrium (LTE) conditions and used the following Equation (see Eq. (A4) of Caselli et al. 2002) to estimate the column density of the species:

$$\frac{dN_{^{13}\text{CO}}(v)}{dv} = \frac{8\pi\nu^3}{c^3} \frac{g_l}{A_{ul} g_u} \frac{Q_{\text{rot}}(T_{\text{ex}})}{1 - \exp(-h\nu/[kT_{\text{ex}}])} \frac{\tau_\nu}{g_l \exp(-E_l/[kT_{\text{ex}}])}, \quad (2)$$

where ν is the frequency of the transition, that is, 110.2 GHz and 220.4 GHz for $^{13}\text{CO}(1-0)$ and $(2-1)$ respectively, A_{ul} is the Einstein coefficient for spontaneous emission ($6.3324 \times 10^{-8} \text{ s}^{-1}$ for $J = 1 \rightarrow 0$ and $6.0745 \times 10^{-7} \text{ s}^{-1}$ for $J = 2 \rightarrow 1$), g_l and g_u are the statistical weights of the lower and upper levels, respectively, Q_{rot} is the rotational partition function, E_l is the energy of the lower state in the transition, and τ is the optical depth. All spectroscopic parameters were obtained from the catalogue of the Cologne Database for Molecular Spectroscopy³ and are listed in

¹ <https://publicwiki.iram.es/Iram30mEfficiencies>

² See <https://www.iram.fr/IRAMFR/GILDAS>

³ <https://cdms.astro.uni-koeln.de>

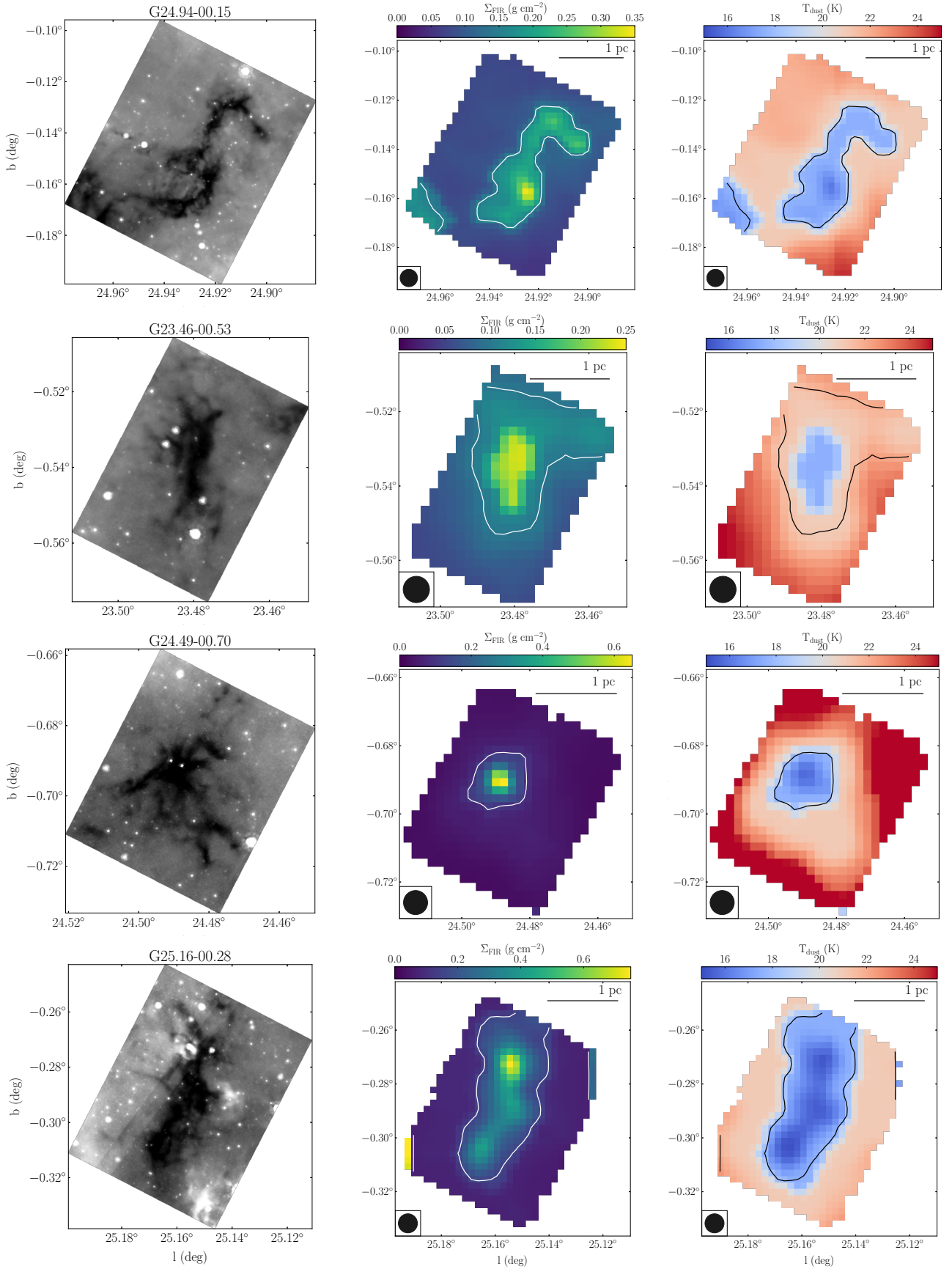


Fig. 1. *Spitzer* 8 μm images (left column), *Herschel*-derived mass surface density maps (Σ ; middle column) and dust temperature (T_{dust} ; right column) for the four IRDCs. In the middle and right panels, the $\Sigma=0.1 \text{ g cm}^{-2}$ black contours highlight the shape of each cloud. The beam size (bottom left) and 1 pc scale bar (top right) are also indicated.

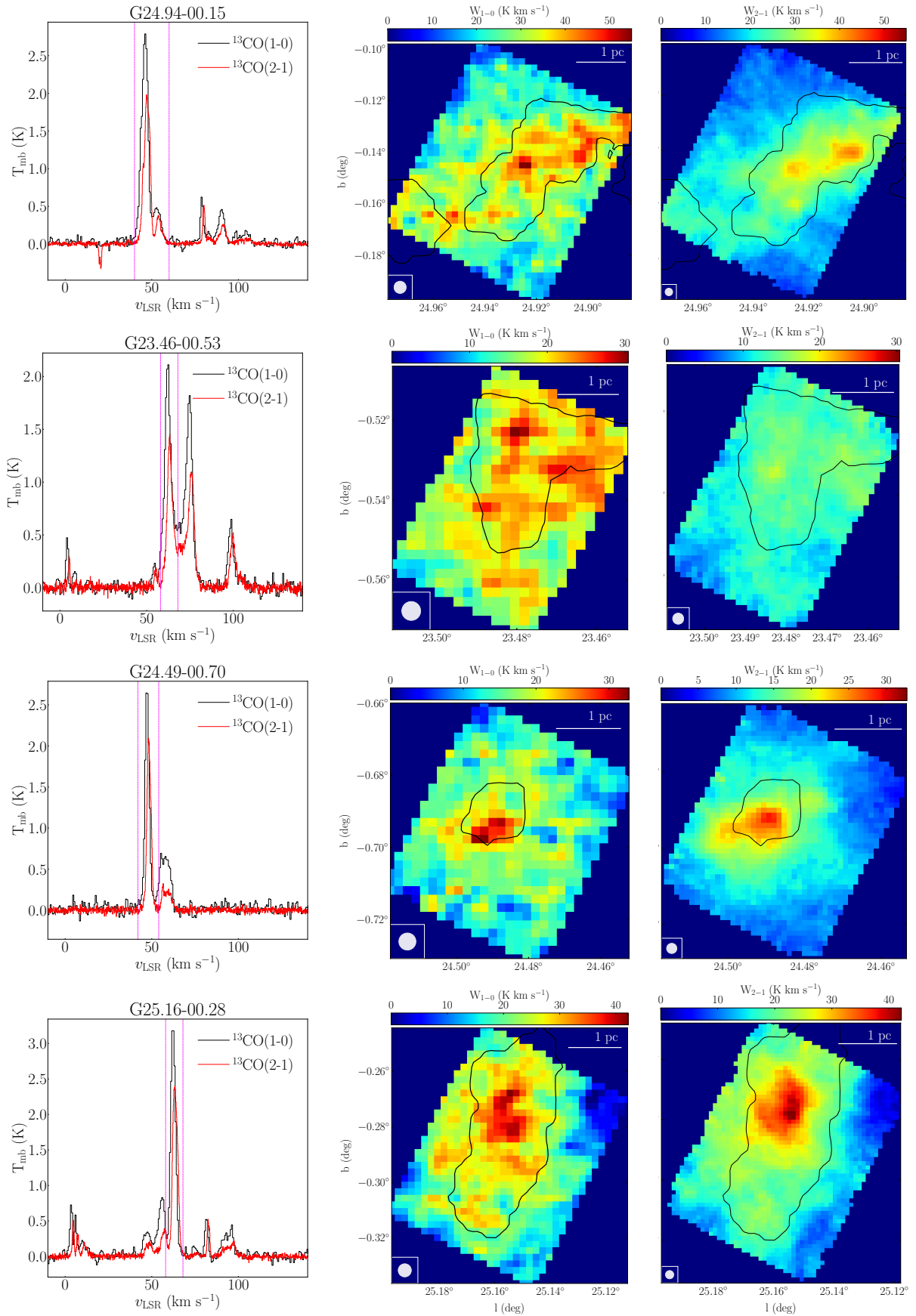


Fig. 2. *Left column:* $^{13}\text{CO}(1-0)$ (black) and $^{13}\text{CO}(2-1)$ (red) spectra averaged towards the full IRDC maps. The velocity ranges considered for each cloud are indicated with vertical dotted magenta lines and are reported in Table 2. *Middle and left columns:* integrated intensity maps of the $^{13}\text{CO}(1-0)$ and $^{13}\text{CO}(2-1)$ obtained over the defined velocity ranges. In both sets of panels, the beam sizes and 1 pc scale bar are indicated.

Table 2. Properties of the four IRDCs and observed maps.

Cloud	l (°)	b (°)	Off pos. (" , ")	Map (' × ')	rms ₁₋₀ (K)	rms ₂₋₁ (K)	Δv (km s ⁻¹)	A_{rms}^{1-0} (K km s ⁻¹)	A_{rms}^{2-1} (K km s ⁻¹)	d_k (kpc)	d_{GC} (kpc)	$^{12}\text{C}/^{13}\text{C}$
G24.94-00.15	24.93	-0.15	-757,87	5 × 4	0.6	0.20	40–60	2.5	0.6	3.0	5.5	53
G23.46-00.53	23.48	-0.54	735,-9	3.5 × 2.5	0.6	0.20	58–68	1.3	0.5	3.8	4.9	49
G24.49-00.70	24.48	-0.70	1050,41	3.5 × 3	0.6	0.14	42-54	1.7	0.4	3.2	5.4	52
G25.16-00.28	25.16	-0.29	2550,5	4.5 × 3.5	0.6	0.20	58–68	2.0	0.6	3.8	4.9	50

Notes. IRDC name, Galactic coordinate, off position, map size, rms per channel per pixel in the ¹³CO(1–0) and ¹³CO(2–1) maps in units of the main-beam temperature, ¹³CO emission velocity range and corresponding integrated noise, kinematic and galactocentric distances, ¹²C/¹³C ratio.

Table 3. Spectroscopic information for the ¹³CO(1–0) and (2–1) transitions.

Transition	Frequency (GHz)	A_{ul} (10 ⁻⁸ s ⁻¹)	g_u	E_l (K)
¹³ CO(1–0)	110.201	6.3324	3	0.00
¹³ CO(2–1)	220.399	60.745	5	5.29

Table 3 (except for g_u , which cancels out in Eq. (2)). We used the following expression for Q_{rot} :

$$Q_{\text{rot}} = \sum_{J=0}^{\infty} (2J+1) \exp(-E_J/[kT_{\text{ex}}]), \quad (3)$$

with $E_J = J(J+1)hB$, where B is the ¹³CO rotational constant 55101.011 MHz⁴.

The optical depth, τ_ν , in Eq. (2) was estimated via

$$T_{B,\nu} = \frac{h\nu}{k} [f(T_{\text{ex}}) - f(T_{\text{bg}})] (1 - e^{-\tau_\nu}). \quad (4)$$

Here, $T_{B,\nu}$ is the main-beam brightness temperature at each velocity (or frequency), $f(T) \equiv [\exp(h\nu/[kT]) - 1]^{-1}$, and $T_{\text{bg}} = 2.73$ K is the background temperature, which we assumed to be the cosmic microwave background temperature.

In these relations (Equations (2) to (4)), the ¹³CO column densities estimated from the two transitions independently need to be the same. Furthermore, it is necessary to know the excitation temperature, T_{ex} , which is the same for both transitions in the adopted LTE conditions. Hence, we estimated T_{ex} at each l, b, v element of the data cube (also known as voxel) as the value for which the ratio of the two ¹³CO column densities converges to unity, that is, $R_{2,1} = dN_{^{13}\text{CO},2,1}/dN_{^{13}\text{CO},1,0} = 1$. We first considered all the voxels for which both transitions had emission above three times the rms and calculated their $R_{2,1}$ assuming $T_{\text{ex}} = 30$ K. Next, we iteratively decreased T_{ex} until $R_{2,1}$ converged to unity. We calculated the two column densities and also accounted for optical depth. For all voxels in which one or both transitions were below three times the rms threshold, we estimated T_{ex} to be the same as the average of that of the local l, b position, that is, for a fixed l, b , we averaged all the channels in which T_{ex} values were estimated and assigned the obtained mean value to channels (within the same l, b element) for which an estimate was not possible. We thus obtained a cube of T_{ex} that we then used to estimate the ¹³CO column density towards each voxel. For the subsequent analysis, we used the ¹³CO column density cubes

⁴ <https://spec.jpl.nasa.gov>

estimated from the ¹³CO(2–1) transition. We note, however, that the ¹³CO column density cubes estimated from the two transitions for each cloud are consistent within the uncertainty, and this choice does not affect the validity of our results.

The 3D column density cubes obtained with the method described above were then converted into 2D maps of $N_{^{13}\text{CO}}$ by summing the contributions at each v channel. Finally, we used these $N_{^{13}\text{CO}}$ maps to estimate the total mass surface density, $\Sigma_{^{13}\text{CO}}$ using the following equation:

$$\Sigma_{^{13}\text{CO}} = \frac{\mu_{\text{H}}}{\chi_{\text{CO}}} \frac{^{12}\text{C}}{^{13}\text{C}} N_{^{13}\text{CO}}, \quad (5)$$

where $\chi_{\text{CO}} = 1.4 \times 10^{-4}$ is the fiducial CO abundance with respect to H nuclei (Frerking et al. 1982), $\mu_{\text{H}} = 2.34 \times 10^{-24}$ g is the mass per H nucleus, and $^{12}\text{C}/^{13}\text{C}=51$ is the ratio of these C isotopes. For this ratio, we adopted the following relation from Milam et al. (2005), which assumes $d_{\text{GC},0} = 8.0$ kpc:

$$\frac{^{12}\text{C}}{^{13}\text{C}} = 6.2(\pm 1.0)(d_{\text{GC}}/\text{kpc}) + 18.7(\pm 7.4), \quad (6)$$

where d_{GC} is the galactocentric distance, estimated from the kinematic distances of the clouds (Simon et al. 2006). As reported in Table 2, we found d_{GC} in the range of 4.9–5.5 kpc and ¹²C/¹³C isotopic ratios between 49 and 52. Because these values are similar, we assumed for simplicity that all the clouds had a ¹²C/¹³C isotopic ratio 51, that is, that they corresponded to the mean of the derived values. We note that from Equation (6), the uncertainty on the isotopic ratio is $\sim 25\%$.

The ¹³CO column density map, T_{ex} column density-weighted map, and ¹³CO-derived mass surface density map for each IRDC are shown in Figure 3. Towards all sources, we found T_{ex} in the range 5–10 K, with average values between 6 and 7 K (see Table 4), $N_{^{13}\text{CO}}$ up to 6×10^{16} cm⁻², and $\Sigma_{^{13}\text{CO}}$ up to 0.04 g cm⁻². These values are similar to those previously obtained towards cloud H by Hernandez et al. (2011) using the same method.

With the above method, we also estimated the optical depth for each ¹³CO transition, τ_{10} , and τ_{21} . The two transitions have optical depths in the range 0.01–3 overall, with an average τ across the clouds of $\langle \tau_{10} \rangle \sim 0.3$ –0.4 and $\langle \tau_{21} \rangle \sim 0.5$ –0.7 for ¹³CO(1–0) and (2–1), respectively. These values are reported in Table 4.

The uncertainties of the quantities derived above are both statistical due to measurement noise and systematic. For T_{ex} , we assumed its uncertainty to be 1 K at $T_{\text{ex}}=7$ K, which was the level adopted by Hernandez et al. (2011). This corresponds to a $\sim 15\%$ uncertainty in the τ and, in turn, to an uncertainty of $\sim 25\%$ in the ¹³CO column densities. To this, we summed in quadrature an additional $\sim 3\%$ uncertainty due to the rms, which thus

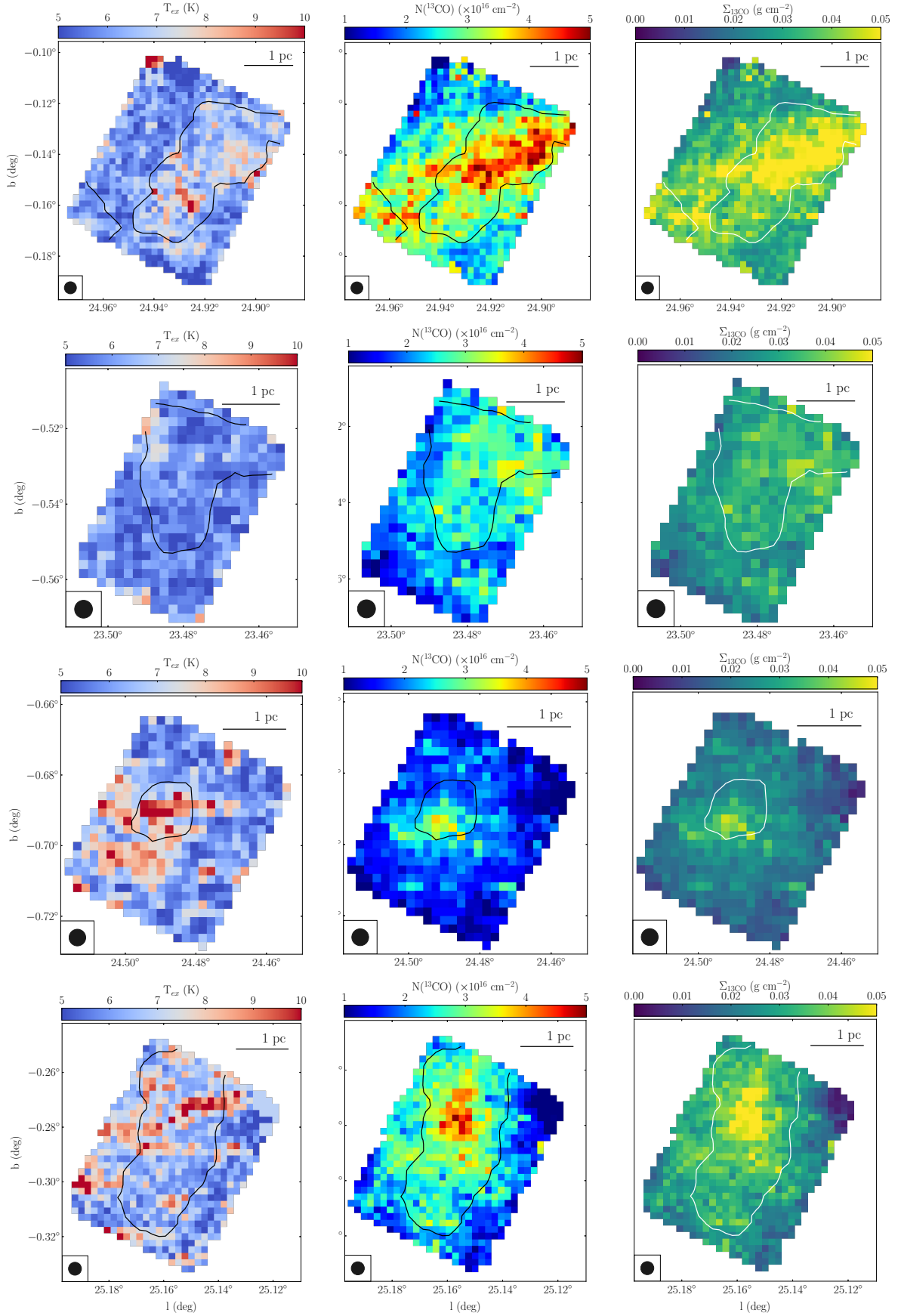


Fig. 3. Maps of the column-density-weighted excitation temperature (*left column*), ^{13}CO column density (*middle column*), and ^{13}CO -derived mass surface density (*right column*) obtained for the four IRDCs (the top to bottom rows show G24.94-00.15, G23.46-00.53, G24.49-00.70, and G25.16-00.28). In each panel, the black contour corresponds to the FIR-derived mass surface density of 0.1 g cm^{-2} .

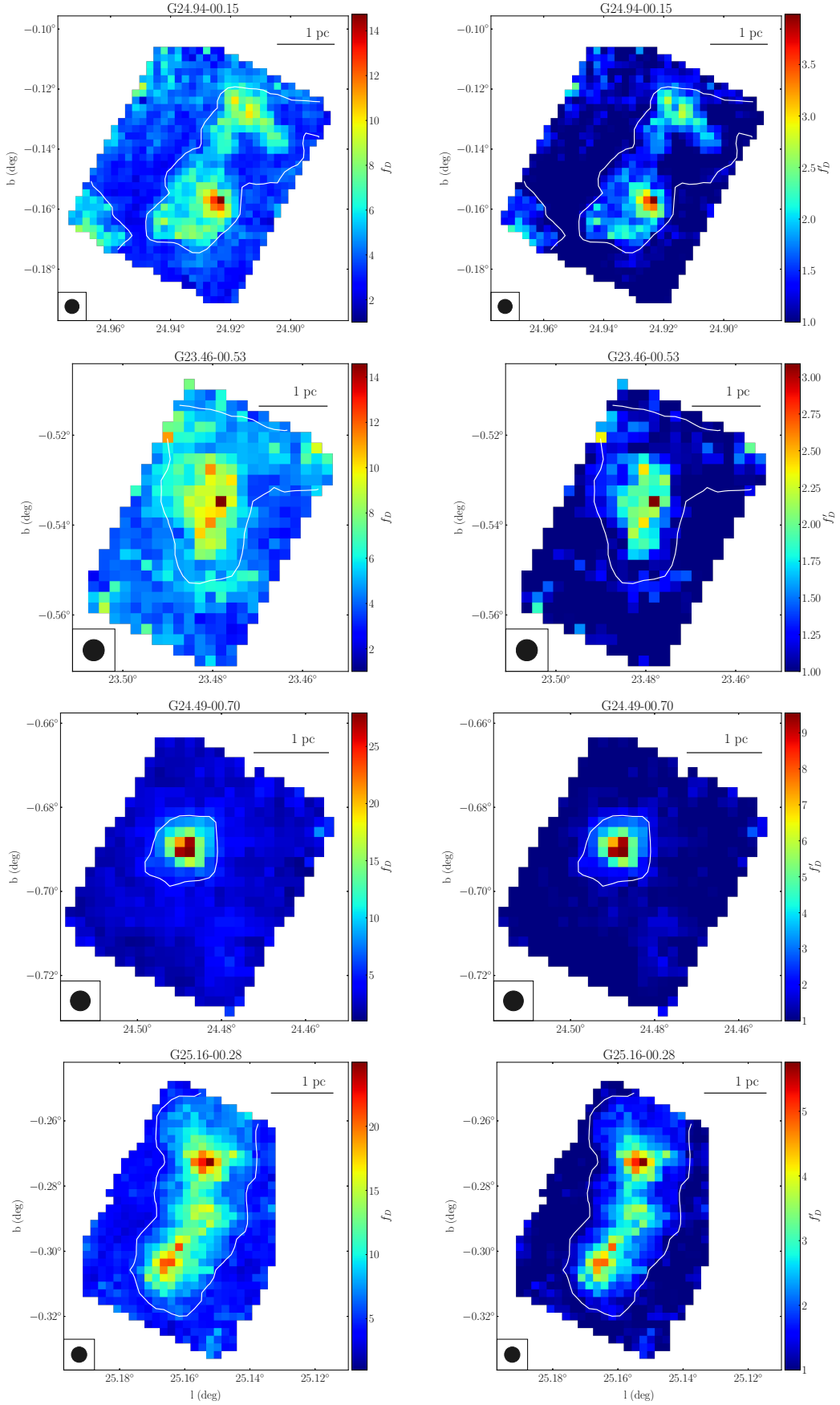


Fig. 4. CO depletion factor (*left column*) and corrected CO depletion factor (*right column*). In each panel, the white contours mark $\Sigma_{\text{FIR}} = 0.1 \text{ g cm}^{-2}$. The beam size and 1 pc scale are indicated in the bottom left and top right corner, respectively.

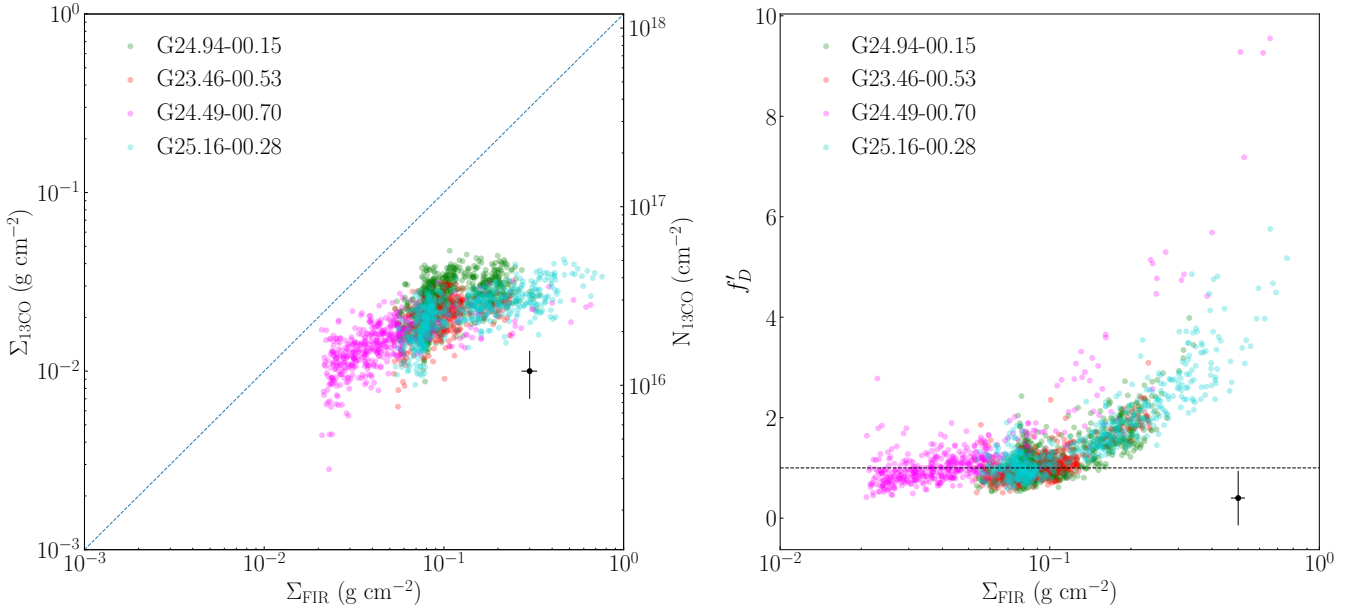


Fig. 5. *Left:* ^{13}CO -derived mass surface density, $\Sigma_{^{13}\text{CO}}$, as a function of the *Herschel*-derived mass surface density, Σ_{FIR} , for all clouds in our sample (different colours). The dotted line corresponds to the one-to-one line. *Right:* normalised CO depletion factor, $f_{D,\text{CO}}$, as a function of the *Herschel*-derived mass surface density, Σ_{FIR} , for all clouds in our sample (different colours). The dotted horizontal line corresponds to $f'_{D,\text{CO}}=1$. The black points represent the average uncertainties in the quantities.

Table 4. Average values extracted for all four IRDCs.

Cloud	$\langle T_{\text{ex}} \rangle$ (K)	$\langle \tau_{10} \rangle$	$\langle \tau_{21} \rangle$	β	f_D	f'_D
G24.94-00.15	6.4	0.3	0.6	3.7	6	1.6
G23.46-00.53	5.8	0.4	0.6	4.7	7	1.5
G24.49-00.70	6.8	0.4	0.7	2.9	15	5
G25.16-00.28	7.0	0.3	0.6	4.3	11	2.5

Notes. Column density-weighted T_{ex} and τ , f_D normalisation factors, *Herschel* mass surface density-weighted CO depletion factor, and normalised CO depletion factor. The average CO depletion factors (normalised and non-normalised) were obtained by considering pixels with $\Sigma_{\text{FIR}} \geq 0.1 \text{ g cm}^{-2}$.

was a very minor contribution, so that the final uncertainty on the column density was $\sim 25\%$. Next, we summed in quadrature the uncertainty arising from the adopted isotopic ratio and other quantities needed to derive $\Sigma_{^{13}\text{CO}}$, for which we then estimated a total overall uncertainty of $\sim 35\%$. The *Herschel* far-infrared (FIR)-derived Σ also has an uncertainty of $\sim 30\%$, as reported by Lim et al. (2016).

4.3. CO depletion

In Figure 5, we show a scatter plot of $\Sigma_{^{13}\text{CO}}$ versus Σ_{FIR} for all the pixels in the maps of IRDCs O, V, X, and Y. The ^{13}CO -derived mass surface densities are in the range $0.003\text{--}0.05 \text{ g cm}^{-2}$. While $\Sigma_{^{13}\text{CO}}$ increases with Σ_{FIR} , it remains systematically lower by factors of $\sim 3\text{--}25$, and this factor grows towards the high- Σ regime. This discrepancy between $\Sigma_{^{13}\text{CO}}$ and Σ_{FIR} might be evidence of CO depletion. Alternatively, other factors might cause a systematic underestimation of Σ via ^{13}CO emission or an overestimation via FIR dust continuum emission.

One potential explanation that was also discussed by Hernandez et al. (2012) is that a strong negative excitation

temperature gradient from the more diffuse to the denser regions of the clouds might cause $\Sigma_{^{13}\text{CO}}$ to be underestimated. As shown in Figure 3, however, we observe no such trend in any of the IRDCs. In contrast, we see indications of a rise of T_{ex} towards the denser regions.

Local fractionation of the ^{13}CO isotope might also explain the low values of $\Sigma_{^{13}\text{CO}}$. Two possible mechanisms might account for this: isotope-selective photo-dissociation, and chemical fractionation. For isotope-selective photo-dissociation, however, the effect is known to be negligible for H volume densities $> 10^2 \text{ cm}^{-3}$ (Szűcs et al. 2014), with this limit well below the average IRDC densities in our clouds. Chemical fractionation, on the other hand, is predicted to become effective for ^{12}CO column densities in the range $10^{15}\text{--}10^{17} \text{ cm}^{-2}$. At the considered $^{12}\text{C}/^{13}\text{C}$ ratio of 51, this corresponds to ^{13}CO column densities in the range $2 \times 10^{13}\text{--}2 \times 10^{15} \text{ cm}^{-2}$. Towards the four IRDCs, we estimate $N_{^{13}\text{CO}} \geq 10^{16} \text{ cm}^{-2}$, and while chemical fractionation might occur to some extent, it is therefore most likely not the main cause of the low $\Sigma_{^{13}\text{CO}}$ we obtained. Moreover, recent simulations also suggested new exchange reactions that might increase the production of ^{13}CO for molecules produced from atomic C (Colzi et al. 2020).

Finally, the dust opacity assumptions adopted by Lim et al. (2016) might affect the Σ_{FIR} estimates. The effects of these assumptions are already considered in the 30% uncertainty reported by the authors and can only account for a small fraction of the Σ_{FIR} variations. In light of all this, we conclude that the relatively low values of $\Sigma_{^{13}\text{CO}}$ are primarily due to the depletion of CO from the gas phase onto dust grains.

To quantify CO depletion, following previous studies (e.g. Caselli et al. 1999; Fontani et al. 2006; Hernandez et al. 2011; Jiménez-Serra et al. 2014), we defined the CO depletion factor as

$$f_D \equiv \frac{\Sigma_{\text{CO,expected}}}{\Sigma_{\text{CO,observed}}} = \frac{\Sigma_{\text{FIR}}}{\Sigma_{^{13}\text{CO}}}. \quad (7)$$

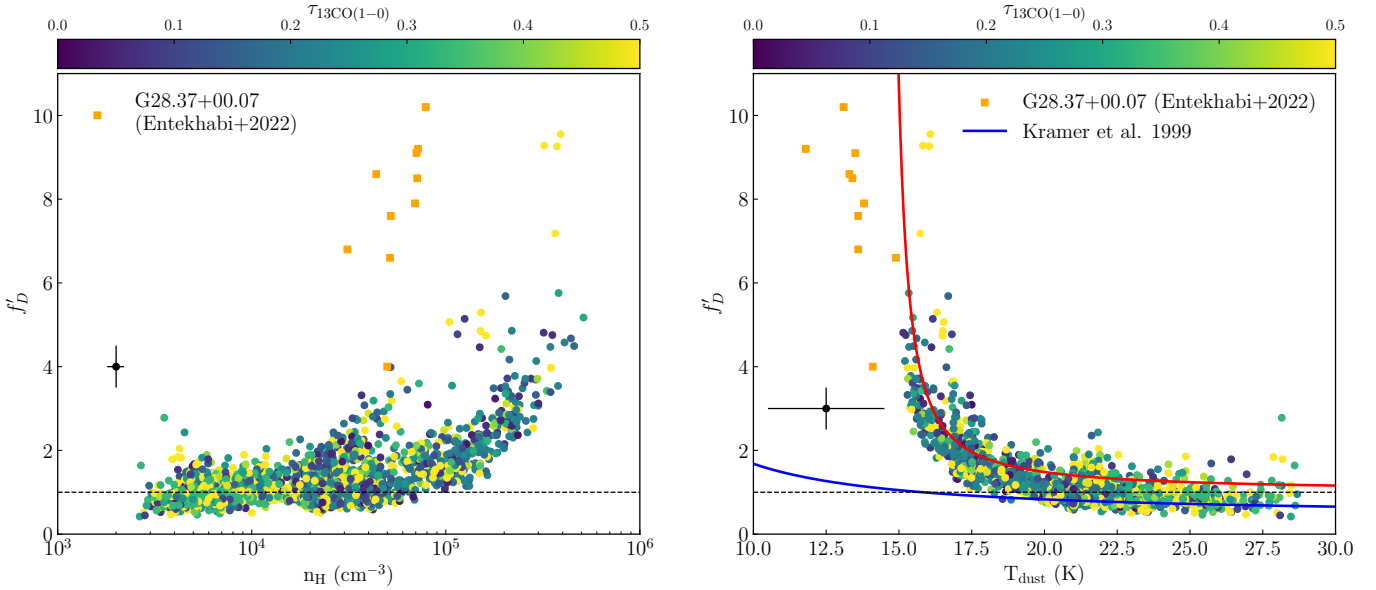


Fig. 6. Corrected CO depletion factors, f'_D , as a function of gas density (i.e. number density of H nuclei, n_H ; left panel) and dust temperature (right panel). We also report the CO depletion values measured by Entekhabi et al. (2022) in Cloud C as orange squares. In both panels, the horizontal dotted black line corresponds to $f'_D = 1$. In the right panel, we also show the empirical relation reported by Kramer et al. (1999) that was derived in the low-mass core IC 5146 (blue curve) (see Eq. (1)). We also show our derived IRDC depletion relation (see Eq. (8)) (red curve).

The corresponding CO depletion maps are shown in Figure 4. In order to take the systematic uncertainties due to the assumed CO abundance and the *Herschel*-derived Σ_{FIR} into account, we re-normalised f_D , so that it was ~ 1 for $T_{\text{dust}} \geq 20$ K, that is, the CO freeze-out temperature (Caselli et al. 1999). We note that this temperature roughly corresponds to a value of $\Sigma \sim 0.1 \text{ g cm}^{-2}$ for all the clouds. We indicate this normalised CO depletion factor as $f'_{D,\text{CO}} = \beta f_D$ and show the obtained maps in Figure 4. For each cloud, the normalisation factors, β , are reported in Table 4, along with the column-density-weighted mean excitation temperatures.

Figure 4 shows that the CO depletion factor takes values $f_D \sim 3\text{--}25$ or $f'_D \sim 1\text{--}9$ after normalisation. For an average cloud kinematic distance of 3 kpc (Table 2), the $8.5''$ pixel scale in our maps corresponds to ~ 0.125 pc and contains $7.4 \times (\Sigma_{13\text{CO}}/0.1 \text{ g cm}^{-2}) M_{\odot}$. Hence, several tens of solar masses per pixel are missed when using CO observations when depletion is not taken into account.

The CO depletion values shown in Figure 4 are consistent with those reported by previous studies of IRDCs within the sample by Butler & Tan (2012). Hernandez et al. (2011) reported normalised CO depletion factors up to 5 towards IRDC G035.39-00.33 (cloud H in Butler & Tan 2012), using C^{18}O emission. Towards the same source, Jiménez-Serra et al. (2014) obtained f_D up to 12 from a non-LTE analysis of the ^{13}CO emission. Entekhabi et al. (2022) used astrochemical models to infer the CO depletion factors towards ten massive clumps in IRDC G028.37 (cloud C in Butler & Tan 2012). For these regions, Entekhabi et al. (2022) reported f_D up to 10, which is slightly higher than the values reported here. The dust temperatures in the ten clumps we studied in cloud C are colder, however, as discussed further below. Sabatini et al. (2019) reported $f_D \leq 6$ towards IRDC G351.77-0.51, which is similar to our f'_D values. Our normalised CO depletion estimates are also consistent with those measured towards high-mass star-forming clumps by Feng et al. (2020) (up to 15) and Fontani et al. (2012), that is, ≤ 10 for a sub-sample of clumps located at distances similar to our sources.

We also investigated how the CO depletion factor varied as a function of the cloud properties of H number density and dust temperature, as shown in Figure 6. Here, we also included the f_D values measured by Entekhabi et al. (2022) in IRDC G28.37 (Cloud C). The H number densities shown in Figure 6 were obtained by applying the machine-learning denoising diffusion probabilistic model described by Xu et al. (2023) to the *Herschel*-derived mass surface density maps. For a detailed description of the method, we refer to Xu et al. (2023). As shown in Figure 6, the CO depletion factor exhibits clear trends as a function of n_H and T_{dust} . In particular, denser and colder regions show higher levels of CO depletion. The scatter in the relation of f_D with density is relatively high, especially if the cloud C were also considered. On the other hand, the relation of CO depletion with temperature follows a monotonic relation more tightly.

The correlation between the large-scale CO depletion in IRDCs and the cloud properties was considered in previous works (e.g. Kramer et al. 1999; Fontani et al. 2011; Sabatini et al. 2019). These studies generally reported evidence of a correlation between n_H and f_D that is broadly consistent with our results. Only Fontani et al. (2011) observed a slight anti-correlation between the two quantities, but also suggested this might be due to beam-dilution effects. Kramer et al. (1999) and Sabatini et al. (2019) also investigated the relation between f_D and T_{dust} for low-mass star-forming regions and IRDCs, respectively, and reported qualitatively similar trends to our results.

In the right panel of Figure 6, we show the functional form of $f_D(T_{\text{dust}})$ derived by Kramer et al. (1999) (see Eq. (1)). It does not track the rapid rise of f_D , which occurs at $T_{\text{dust}} \lesssim 18$ K. This might reflect real differences in the molecular cloud environments between the low-mass core IC 5146 and our IRDC sample: especially the range of Σ in the low-mass core is much smaller, that is, $\Sigma \lesssim 0.1 \text{ g cm}^{-2}$, than our IRDCs, where $0.1 \text{ g cm}^{-2} \lesssim \Sigma \lesssim 0.7 \text{ g cm}^{-2}$. Alternatively, as mentioned in §1, systematic uncertainties in measurement of T_{dust} might be at play.

In Figure 6, we also present a new functional form for $f'_D(T_{\text{dust}})$ that is a better description of IRDC conditions (taking the uncertainties on f'_D and T_{dust} into account),

$$f'_D = \exp\left[\frac{T_0}{(T_{\text{dust}} - T_1)}\right]. \quad (8)$$

The example curve shown in Fig. 6 has $T_0 = 4$ K and $T_1 = 12$ K. The validity in the temperature range is ~ 15 K $\lesssim T_{\text{dust}} \lesssim 30$ K. The main feature of the relation is the rapid rise of the depletion factor at temperatures $\lesssim 18$ K.

These results suggest overall that the dust temperature and not the density is the most important variable in controlling the CO depletion factor. In addition, the relatively small amount of scatter seen in the $f'_D(T_{\text{dust}})$ relation might indicate that CO depletion has reached a near equilibrium value, that is, a balance in the rates of freeze-out and desorption, with the latter being dominated by thermal desorption and not by non-thermal (e.g. cosmic-ray induced) desorption processes. We anticipate that these results will be important constraints for astrochemical models of molecular clouds (see also Entekhabi et al. 2022) and for their chemodynamical history (e.g. Hsu et al. 2023).

5. Conclusions

We have used $^{13}\text{CO}(1-0)$ and $(2-1)$ observations to infer the levels of CO depletion towards a sample of four IRDCs. We found normalised CO depletion factors up to 10 that cannot be explained by systematic uncertainties in our analysis or chemical effects alone. We found that CO depletion generally increases with increasing cloud density, although with significant scatter. There is a tighter correlation with the dust temperature, with CO depletion rising rapidly for $T_{\text{dust}} \lesssim 18$ K. To capture this behaviour, we proposed a functional form for the normalised CO depletion factor of $f'_D = A \exp(T_0/[T_{\text{dust}} - T_1])$ with values of the coefficients $T_0 \approx 4$ K and $T_1 \approx 12$ K. These results indicate overall that the dust temperature is the most important variable in controlling the CO depletion factor. The relatively small amount of scatter might indicate that the level of gas-phase CO has reached near equilibrium values, with thermal desorption playing a dominant role in balancing freeze-out. These results provide important constraints for astrochemical models and for the chemodynamical history of gas during the early stages of star formation.

Acknowledgements. G.C. acknowledges support from the Swedish Research Council (VR Grant; Project: 2021-05589). J.C.T. acknowledges support from ERC project 788829 (MSTAR). I.J.-S. acknowledges funding from grant PID2022-136814NB-I00 funded by the Spanish Ministry of Science, Innovation and Universities/State Agency of Research MICIU/AEI/10.13039/501100011033 and by “ERDF/EU”. J.D.H. gratefully acknowledges financial support from the Royal Society (University Research Fellowship; URF/R1/221620). S.V. acknowledges partial funding from the European Research Council (ERC) Advanced Grant MOPPEX 833460. This work is based on observations carried out under project number 013-20 with the IRAM 30m telescope. IRAM is supported by INSU/CNRS (France), MPG (Germany) and IGN (Spain). This publication makes use of data from FUGIN, FOREST Unbiased Galactic plane Imaging survey with the Nobeyama 45-m telescope, a legacy project in the Nobeyama 45-m radio telescope.

References

Butler, M. J., & Tan, J. C. 2009, *ApJ*, 696, 484
Butler, M. J., & Tan, J. C. 2012, *ApJ*, 754, 5

- Caselli, P., Walmsley, C. M., Tafalla, M., Dore, L., & Myers, P. C. 1999, *ApJ*, 523, L165
Caselli, P., Benson, P. J., Myers, P. C., & Tafalla, M. 2002, *ApJ*, 572, 238
Caselli, P., Vastel, C., Ceccarelli, C., et al. 2008, *A&A*, 492, 703
Christie, H., Viti, S., Yates, J., et al. 2012, *MNRAS*, 422, 968
Churchwell, E., Babler, B. L., Meade, M. R., et al. 2009, *PASP*, 121, 213
Clarke, S. D., Makeev, V. A., Sánchez-Monge, Á., et al. 2024, *MNRAS*, 528, 1555
Colzi, L., Sipilä, O., Roueff, E., Caselli, P., & Fontani, F. 2020, *A&A*, 640, A51
Crapsi, A., Caselli, P., Walmsley, C. M., et al. 2005, *ApJ*, 619, 379
Dalgarno, A., & Lepp, S. 1984, *ApJ*, 287, L47
Egan, M. P., Shipman, R. F., Price, S. D., et al. 1998, *ApJ*, 494, L199
Entekhabi, N., Tan, J. C., Cosentino, G., et al. 2022, *A&A*, 662, A39
Feng, S., Li, D., Caselli, P., et al. 2020, *ApJ*, 901, 145
Fontani, F., Caselli, P., Crapsi, A., et al. 2006, *A&A*, 460, 709
Fontani, F., Palau, A., Caselli, P., et al. 2011, *A&A*, 529, L7
Fontani, F., Giannetti, A., Beltrán, M. T., et al. 2012, *MNRAS*, 423, 2342
Ford, A. B., & Shirley, Y. L. 2011, *ApJ*, 728, 144
Fortune-Bashee, X., Sun, J., & Tan, J. C. 2024, *ApJ*, 977, L6
Foster, J. B., Arce, H. G., Kassisi, M., et al. 2014, *ApJ*, 791, 108
Frerking, M. A., Langer, W. D., & Wilson, R. W. 1982, *ApJ*, 262, 590
Gong, Y., Belloche, A., Du, F. J., et al. 2021, *A&A*, 646, A170
Herbst, E., & van Dishoeck, E. F. 2009, *ARA&A*, 47, 427
Hernandez, A. K., & Tan, J. C. 2015, *ApJ*, 809, 154
Hernandez, A. K., Tan, J. C., Caselli, P., et al. 2011, *ApJ*, 738, 11
Hernandez, A. K., Tan, J. C., Kainulainen, J., et al. 2012, *ApJ*, 756, L13
Hirata, Y., Kawamura, A., Nishimura, A., et al. 2024, *PASJ*, 76, 65
Hsu, C.-J., Tan, J. C., Holdship, J., et al. 2023, arXiv e-prints [arXiv:2308.11803]
Inutsuka, S.-i., Inoue, T., Iwasaki, K., & Hosokawa, T. 2015, *A&A*, 580, A49
Jiménez-Serra, I., Caselli, P., Fontani, F., et al. 2014, *MNRAS*, 439, 1996
Kainulainen, J., & Tan, J. C. 2013, *A&A*, 549, A53
Kong, S., Caselli, P., Tan, J. C., Wakelam, V., & Sipilä, O. 2015, *ApJ*, 804, 98
Kong, S., Tan, J. C., Caselli, P., et al. 2017, *ApJ*, 834, 193
Kramer, C., Alves, J., Lada, C. J., et al. 1999, *A&A*, 342, 257
Li, Q., Tan, J. C., Christie, D., Bisbas, T. G., & Wu, B. 2018, *PASJ*, 70, S56
Lim, W., Tan, J. C., Kainulainen, J., Ma, B., & Butler, M. J. 2016, *ApJ*, 829, L19
Milam, S. N., Savage, C., Brewster, M. A., Ziurys, L. M., & Wyckoff, S. 2005, *ApJ*, 634, 1126
Morii, K., Sanhueza, P., Nakamura, F., et al. 2021, *ApJ*, 923, 147
Moser, E., Liu, M., Tan, J. C., et al. 2020, *ApJ*, 897, 136
Perault, M., Omont, A., Simon, G., et al. 1996, *A&A*, 315, L165
Peretto, N., Lenfestey, C., Fuller, G. A., et al. 2016, *A&A*, 590, A72
Pillai, T., Wyrowski, F., Carey, S. J., & Menten, K. M. 2006, *A&A*, 450, 569
Pillai, T., Kauffmann, J., Zhang, Q., et al. 2019, *A&A*, 622, A54
Rathborne, J. M., Jackson, J. M., & Simon, R. 2006, *ApJ*, 641, 389
Redaelli, E., Bovino, S., Giannetti, A., et al. 2021, *A&A*, 650, A202
Redaelli, E., Bovino, S., Sanhueza, P., et al. 2022, *ApJ*, 936, 169
Retes-Romero, R., Mayya, Y. D., Luna, A., & Carrasco, L. 2020, *ApJ*, 897, 53
Sabatini, G., Giannetti, A., Bovino, S., et al. 2019, *MNRAS*, 490, 4489
Sabatini, G., Bovino, S., Giannetti, A., et al. 2020, *A&A*, 644, A34
Sabatini, G., Bovino, S., Sanhueza, P., et al. 2022, *ApJ*, 936, 80
Sabatini, G., Bovino, S., Redaelli, E., et al. 2024, *A&A*, 692, A265
Simon, R., Rathborne, J. M., Shah, R. Y., Jackson, J. M., & Chambers, E. T. 2006, *ApJ*, 653, 1325
Socci, A., Caselli, P., Sipilä, O., et al. 2024, *A&A*, 687, A70
Suwannajak, C., Tan, J. C., & Leroy, A. K. 2014, *ApJ*, 787, 68
Szűcs, L., Glover, S. C. O., & Klessen, R. S. 2014, *MNRAS*, 445, 4055
Tan, J. C. 2000, *ApJ*, 536, 173
Tan, J. C. 2010, *ApJ*, 710, L88
Tan, J. C., Kong, S., Butler, M. J., Caselli, P., & Fontani, F. 2013, *ApJ*, 779, 96
Tan, J. C., Beltrán, M. T., Caselli, P., et al. 2014, in *Protostars and Planets VI*, eds. H. Beuther, R. S. Klessen, C. P. Dullemond, & T. Henning, 149
Tasker, E. J., & Tan, J. C. 2009, *ApJ*, 700, 358
Umamoto, T., Minamidani, T., Kuno, N., et al. 2017, *PASJ*, 69, 78
Vázquez-Semadeni, E., Palau, A., Ballesteros-Paredes, J., Gómez, G. C., & Zamora-Avilés, M. 2019, *MNRAS*, 490, 3061
Whittet, D. C. B., Goldsmith, P. F., & Pineda, J. L. 2010, *ApJ*, 720, 259
Wu, B., Van Loo, S., Tan, J. C., & Bruderer, S. 2015, *ApJ*, 811, 56
Wu, B., Tan, J. C., Nakamura, F., et al. 2017, *ApJ*, 835, 137
Xu, D., Tan, J. C., Hsu, C.-J., & Zhu, Y. 2023, *ApJ*, 950, 146
Yang, B., Stancil, P. C., Balakrishnan, N., & Forrey, R. C. 2010, *ApJS*, 188, 581
Yu, H., Wang, J., & Tan, J. C. 2020, *ApJ*, 905, 78
Zhang, Q., Wang, Y., Pillai, T., & Rathborne, J. 2009, *ApJ*, 696, 268